A fast-converging scheme for the phonon Boltzmann equation with dual relaxation times

Jia Liu[a], Chuang Zhang[a], Haizhuan Yuan[b], Wei Su[c,*], Lei Wu[a,*]

[a]*Department of Mechanics and Aerospace Engineering, Southern University of Science and Technology, Shenzhen 518055, China*
[b]*School of Mathematics and Computational Science, Xiangtan University, Xiangtan 411105, China*
[c]*School of Engineering, The University of Edinburgh, Edinburgh EH9 3FD, UK*

Abstract

The phonon Boltzmann transport equation with dual relaxation times is often used to describe the heat conduction in semiconductor materials when the classical Fourier's law is no longer valid. For practical engineering designs, accurate and efficient numerical methods are highly demanded for numerically resolving the equation. At large Knudsen numbers (defined as the ratio of the phonon mean free path to a characteristic system length), steady-state solutions can be obtained via the conventional iterative scheme (CIS) within a few iterations. However, when the Knudsen number becomes small, i.e., when the phonon transport occurs in the diffusive or hydrodynamic regime, thousands of iterations are required to obtain converged results. In this work, a general synthetic iterative scheme (GSIS) is proposed to tackle the inefficiency of the CIS. The key ingredient of the GSIS is that a set of macroscopic synthetic equations, which is exactly derived from the Boltzmann transport equation, is simultaneously solved with the kinetic equation to obtain temperature and heat flux. During the iteration, the macroscopic quantities are used to evaluate the equilibria in the scattering terms of the kinetic equation thus guide the evolution of the phonon distribution function, while the distribution function in turn provides closures to the synthetic equations. The Fourier stability analysis is conducted to reveal the superiority of the GSIS over the CIS in terms of fast convergence. It is shown that the convergence rate of the GSIS can be always maintained under 0.2, so that only 2 iterations are required to reduce the iterative error by one order of magnitude. Numerical results are presented to further demonstrate the efficiency of GSIS, where the CPU time is reduced by up to three orders of magnitude, especially in both the diffusive and hydrodynamic regimes.

Keywords: phonon Boltzmann equation; general synthetic iterative scheme; Fourier stability analysis; fast convergence

*Corresponding authors:
Email addresses:* `wei.su@ed.ac.uk` (Wei Su), `wul@sustech.edu.cn` (Lei Wu)

1. Introduction

With the rapid development of semiconductor technology, the characteristic size of micro-electronic devices becomes smaller and smaller. Heat conduction at the micro-/nano-scales has attracted extensive attention [1, 2, 3], as it has vital applications in controlling the heat dissipation of electronic devices and developing thermal functional materials. Although the classical Fourier's law has been guiding the study of heat conduction over the past centuries, it is no longer valid when the Knudsen number is not small, i.e., when the characteristic system length is comparable to or even smaller than the phonon mean free path [4, 5]. A host of interesting phonon transport phenomena beyond the Fourier diffusion picture have been observed in micro-/nano-scale devices and materials [3, 6, 7]. For the mathematical description of such non-Fourier heat conduction, the phonon Boltzmann equation (PBE) should be adopted [8].

The PBE is an integro-differential equation defined in the phase space of seven dimensions [4, 5] including the time t, the spatial coordinates $\boldsymbol{x}$, the phonon angular frequency ω, and the solid angle Ω, which poses a grand research challenge to find its solution accurately and efficiently. Analogous to the kinetic models for rarefied gas flows, the relaxation-time approximation is introduced to simplify the scattering term in the PBE [8, 9]. For example, the approximation of a single-mode relaxation time [5] is commonly used to describe the resistive scattering (conserves energy but not momentum); and it has been shown this approximation can well predict the heat conduction in silicon and germanium. However, for materials in which the normal scattering (conserves both energy and momentum) plays a significant role [6, 10, 11, 12, 13, 14], the single-relaxation-time model is not applicable. To circumvent this problem, Callaway proposed a model with dual relaxation times [15], which assumes that the normal scattering and resistive scattering are equally important and restores the phonon distribution to a displaced Planck distribution and a Planck distribution, respectively.

Two primary methods are used to find solutions to the PBE and its model equations: the derivation of macroscopic equations and direct numerical simulation. For the former one, Guyer and Krumhansl [16] first obtained the Guyer-Krumhansl equations from the linearized PBE. Subsequently, macroscopic equations were derived via the Chapman-Enskog expansion [17] and the moment method [18, 19, 20, 21, 22]. These macroscopic equations are not valid in the whole range of Knudsen numbers: they are only accurate near the diffusive regime where the resistive scattering is strong, and the hydrodynamic regime where the resistive scattering is quite weak but the normal scattering plays an important role. For the direct simulation, efficient and accurate numerical methods are needed since the kinetic equations are defined in the phase-space with high dimensionality.

Many numerical methods including the Monte Carlo scheme [23, 24, 25], the lattice Boltzmann method [26], the discrete ordinate method [27, 28], and the discrete unified gas kinetic scheme [29, 30] have been developed. The Monte Carlo method is a stochastic approach; due to the fact that the advection and scattering of phonons are handled separately, the time step is required to be smaller than the smallest scattering time scale. As a result, the Monte Carlo method is expensive in the diffusive and hydrodynamic regimes. More-

over, it suffers from large statistical errors due to its stochastic nature, especially when the temperature variation is small. To mitigate the latter problem, the variance-reduced Monte Carlo method was proposed, in which only the deviation from the equilibrium state is resolved [31]. However, it is still not efficient in the diffusive or hydrodynamic regime since the restriction on time step is not removed. The standard lattice Boltzmann method, initially proposed for fluid dynamics [32], was extended to solve the PBE. Since it is made on the near-equilibrium hypothesis, this method has difficulties in treating strong nonequilibrium effects and phonon spectral properties. Hence, it can only be adopted at small Knudsen numbers and is unsuitable to capture the non-Fourier heat conduction. In the discrete ordinate method, the phonon frequency and angular variables are first discretized based on a numerical quadrature, resulting in a set of equations that are continuous in the spatial space and time; then the classical numerical techniques are applied to approximate the spatial derivative and time integration. The discrete ordinate method is a deterministic approach, which yields noise-free solutions. However, like the Monte Carlo method, it handles the advection and scattering operators separately; thus, it is, as well, restricted by the requirement of time step and inefficient in small-Knudsen-number regimes. This problem is rectified in the discrete unified gas kinetic scheme, where the advection and scattering are coupled through a sophisticated construction of the numerical flux at spatial cell interfaces, so that large time step can be used.

Although great progresses on numerical simulations have been made in the past decades, the explicit marching strategy widely used in the existing schemes suffers difficulties when dealing with steady heat conduction problems [33, 34, 35, 36]. For example, when the normal scattering is strong while the resistive scattering is weak, the temperature profile changes rapidly in the vicinity of boundaries, while in the bulk region the temperature variation is small, see Fig. 5(b) in this work. For this case, a non-uniform spatial grid is necessarily used to reduce the number of spatial grid cells. However, due to the Courant–Friedrichs–Lewy (CFL) condition, the time step is usually limited by the smallest cell size; thus, a huge number of time steps is required to reach the steady state [4, 5]. Consequently, implicit time-marching method is highly demanded. The conventional iterative scheme (CIS), based on the discrete ordinate method, is an implicit method thus removes the restriction from the CFL condition [33, 37, 38]. When it is adopted to solve the phonon transport equations, the time derivative is dropped and the scattering operator is split into the gain term and the loss term. The advection operator and loss term are calculated at the current iteration step, while the gain term is evaluated at the previous iteration step to avoid inverting large matrix. The iteration terminates until time-independent solutions are achieved. When the Knudsen number is large, the CIS is efficient since the converged solution can be obtained within a few iterations [33, 34, 39]. However, the number of iterations increases dramatically when the Knudsen number becomes small. Therefore, it is necessary to develop a method to accelerate the convergence of CIS, especially in small-Knudsen-number regimes. This is urgently needed for simulating micro-/nano-scale heat conduction problems, where multiscale transport is often encountered. For instance, heat is generated in a small source region and is eventually conducted to a much larger substrate [28].

If the normal scattering is absent, the PBE has the same form as that of the radiation

3

transport, where in the diffusive regime many acceleration methods have been developed, e.g., the diffusion synthetic iterative scheme [37, 40]. The basic idea of the synthetic iterative scheme is that the kinetic equation and a set of macroscopic equations (the diffusion equation when only the resistive scattering is considered) are solved simultaneously: the mesoscopic kinetic equation provides high-order moments to the macroscopic equations, while the macroscopic equations provide the macroscopic quantities appearing in the scattering term. Since the diffusion equation allows very efficient exchanges of information, fast convergence is achieved [41]. When the Callaway model is considered, especially when the normal scattering is strong and the resistive scattering is relatively weak, the limiting equations are no longer the diffusion equation but the Guyer-Krumhansl equations [16]. Therefore, a novel synthetic iterative scheme that is different from the one with only the resistive scattering considered is required. This is the main scope of the present work: to develop and analyze an efficient scheme for the Callaway model and simulate more general phonon transport problems. We name the new scheme as the general synthetic iterative scheme (GSIS). The GSIS has been developed and successfully applied for rarefied gas flows. With the aid of the macroscopic equations that are accurate over the whole flow regime and asymptotically preserve the Navier-Stokes limit, the solutions to the Boltzmann equation for multiscale gas flows can be obtained within dozens of iterations. The GSIS has been developed for linear/nonlinear systems of monatomic and polyatomic gases [42, 43, 44], and recently been extended for unsteady flows. In this work, it is the first time the GSIS is developed for multiscale phonon transport problems. We will focuse on steady-state problems. It is worthy to mention that the propsed algorithm is straightfordly extendible for unsteady cases, where time derivatives in the governing equations will be retained and can be efficiently approximated by some implicit time-marching schemes. When obtaining the transient solution of the PBE from one time to another time, the equation should be solved iteratively since the scattering term is not invertible. This is often called the inner iteration in a time-dependent implicit scheme. Then, the GSIS can be directly applied to accelerate the convergence of the inner iteration between two consecutive transient times.

The remainder of this paper is organized as follows: in section 2, the PEB combining Callawy's dual-relaxation-time model is introduced. In section 3, the CIS for the Callaway model is described and the GSIS to improve the CIS is proposed. The convergence rates of both schemes are rigorously analyzed by the Fourier stability analysis. In section 4, three numerical examples in different phonon transport regimes are simulated to demonstrate the fast convergence of the GSIS. Summaries and outlooks are given in section 5 .

2. Phonon Boltzmann equation: the Callaway model

The heat conduction in semiconductor materials can be modeled as the flow of phonon gas carrying energies, which is described by the PBE for the evolution of phonon distribution function f. Modeling of phonon scattering is rather complicated, and here we consider a simplified version, i.e., the Callaway dual relaxation times model [15, 45]:

$$\frac{\partial f}{\partial t} + \boldsymbol{v} \cdot \boldsymbol{\nabla}_{\boldsymbol{x}} f = \frac{f_{eq}^R - f}{\tau_R} + \frac{f_{eq}^N - f}{\tau_N}, \tag{1}$$

4

where $f(t, \boldsymbol{x}, p, \omega, \boldsymbol{s})$ is a function of the time t, the spatial coordinate $\boldsymbol{x} = (x_1, x_2, x_3)$, the phonon polarization p, the angular frequency ω, and the unit vector along the direction of phonon propagation $\boldsymbol{s} = (\cos\theta, \sin\theta\cos\varphi, \sin\theta\sin\varphi)$ with $\theta \in [0, \pi]$ being the polar angle between $\boldsymbol{s}$ and x_1 axis, and $\varphi \in [0, 2\pi]$ being the azimuthal angle between the projection of $\boldsymbol{s}$ in the $x_2 - x_3$ plane and x_2 axis. The phonon group velocity $\boldsymbol{v} = (v_1, v_2, v_3)$ is defined as

$$\boldsymbol{v} = \boldsymbol{\nabla}_k \omega = |\boldsymbol{v}|\boldsymbol{s}, \tag{2}$$

where $\boldsymbol{k}$ is the wave vector, and the frequency ω can be determined from the dispersion relation $\omega = \omega_p(\boldsymbol{k})$. In this work, we adopt the isotropic hypothesis, i.e., the frequency only depends on the magnitude of the wave vector and is independent on its direction, and take the linear dispersion $\omega = c|\boldsymbol{k}|$; here c is the Debye velocity of the solid. τ_R and τ_N denote the relaxation times of the phonon resistive scattering and normal scattering, respectively. The gray-matter assumption that the relaxation times τ_R and τ_N are constant is employed. f_{eq}^R is the local equilibrium distribution for the resistive scattering, following the Bose-Einstein distribution [46]

$$f_{eq}^R = \frac{1}{\exp\left(\frac{\hbar\omega}{k_B T}\right) - 1}, \tag{3}$$

while f_{eq}^N is the local equilibrium distribution for the normal scattering, following the drifted Bose-Einstein distribution [15]

$$f_{eq}^N = \frac{1}{\exp\left(\frac{\hbar\omega - \hbar\boldsymbol{k}\cdot\boldsymbol{u}}{k_B T}\right) - 1}, \tag{4}$$

where $\hbar$ is the reduced Planck's constant, k_B is the Boltzmann constant, T and $\boldsymbol{u}$ (related to heat flux $\boldsymbol{q}$) are the macroscopic temperature and drift velocity, respectively. According to the energy conservation in both the resistive and normal scatterings, and the momentum conservation in the normal scattering, the equilibrium distribution functions satisfy

$$\text{energy conservation:} \sum_p \iint \hbar\omega \frac{f_{eq}^R - f}{\tau_R} D_p(\omega)\mathrm{d}\Omega\mathrm{d}\omega = 0,$$

$$\sum_p \iint \hbar\omega \frac{f_{eq}^N - f}{\tau_N} D_p(\omega)\mathrm{d}\Omega\mathrm{d}\omega = 0, \tag{5}$$

$$\text{momentum conservation:} \sum_p \iint \hbar\boldsymbol{k} \frac{f_{eq}^N - f}{\tau_N} D_p(\omega)\mathrm{d}\Omega\mathrm{d}\omega = 0,$$

with $D_p(\omega)$ being the phonon density of state.

Consider a phonon system in which the temperature variation around the reference temperature T_0 is small, we expand $f_{eq}^R(T)$ at $T = T_0$ by Taylor's theorem and retain only the first derivation. It becomes

$$f_{eq}^R(T) = f_{eq}^R(T_0) + \frac{\partial f_{eq}^R}{\partial T}(T - T_0). \tag{6}$$

On substituting Eq. (6) into Eq. (1) and introducing the quantity

$$e(t, \boldsymbol{x}, p, \omega, \boldsymbol{s}) = \hbar\omega \frac{D_p(\omega)}{4\pi} \left[f - f_{eq}^R(T_0) \right], \tag{7}$$

the PBE is linearized as

$$\frac{\partial e}{\partial t} + \boldsymbol{v} \cdot \boldsymbol{\nabla_x} e = \frac{e_{eq}^R - e}{\tau_R} + \frac{e_{eq}^N - e}{\tau_N}. \tag{8}$$

The unknown e has the physical meaning of the perturbation of energy density, and the corresponding equilibrium distributions for the resistive and normal scatterings are read as [35]

$$e_{eq}^R = \frac{C_v (T - T_0)}{4\pi}, \quad e_{eq}^N = \frac{C_v (T - T_0)}{4\pi} + \frac{C_v T \boldsymbol{u} \cdot \boldsymbol{s}}{4\pi |\boldsymbol{v}|}, \tag{9}$$

where C_v is the volumetric specific heat capacity defined as

$$C_v = \hbar\omega D_p(\omega) \frac{\partial f_{eq}^R}{\partial T} = \frac{dE}{dT}, \tag{10}$$

with E being the phonon energy. Since the gray model with a single frequency is adopted, according to the conservation laws (5), the macroscopic variables are evaluated from the moments of e as

$$T = \frac{E}{C_v} = \frac{1}{C_v} \int e \mathrm{d}\Omega, \quad \boldsymbol{u} = \frac{3}{C_v T} \int \boldsymbol{v} e \mathrm{d}\Omega, \quad \boldsymbol{q} = \int \boldsymbol{v} e \mathrm{d}\Omega. \tag{11}$$

Introducing the following dimensionless variables

$$\begin{aligned}
\tilde{x} &= \frac{x}{L}, \quad \tilde{\boldsymbol{v}} = \frac{\boldsymbol{v}}{|\boldsymbol{v}|}, \quad \tilde{\boldsymbol{u}} = \frac{\boldsymbol{u}}{|\boldsymbol{v}|}, \quad \tilde{T} = \frac{T - T_0}{T_0}, \quad \tilde{\boldsymbol{q}} = \frac{\boldsymbol{q}}{C_v |\boldsymbol{v}| T_0}, \\
\tilde{e} &= \frac{e}{C_v T_0}, \quad \tilde{e}_{eq}^{R/N} = \frac{e_{eq}^{R/N}}{C_v T_0}, \quad Kn_R = \frac{|\boldsymbol{v}| \tau_R}{L}, \quad Kn_N = \frac{|\boldsymbol{v}| \tau_N}{L},
\end{aligned} \tag{12}$$

Eq. (8) is nondimensionlized as

$$\tilde{\boldsymbol{v}} \cdot \boldsymbol{\nabla}_{\tilde{\boldsymbol{x}}} \tilde{e} = \frac{\tilde{e}_{eq}^R - \tilde{e}}{Kn_R} + \frac{\tilde{e}_{eq}^N - \tilde{e}}{Kn_N}, \tag{13}$$

where the time derivation is dropped since we are interested in the steady-state solution. The dimensionless equilibria are

$$\tilde{e}_{eq}^R = \frac{\tilde{T}}{4\pi}, \quad \tilde{e}_{eq}^N = \frac{\tilde{T}}{4\pi} + \frac{3\tilde{\boldsymbol{q}} \cdot \boldsymbol{s}}{4\pi}, \tag{14}$$

and the dimensionless macroscopic quantities in the scattering operators are evaluated as

$$\tilde{T} = \int \tilde{e} \mathrm{d}\Omega, \quad \tilde{\boldsymbol{u}} = 3 \int \tilde{\boldsymbol{v}} \tilde{e} \mathrm{d}\Omega, \quad \tilde{\boldsymbol{q}} = \int \tilde{\boldsymbol{v}} \tilde{e} \mathrm{d}\Omega. \tag{15}$$

6

In the following sections, the tilde symbol will be omitted without any confusion.

The two dimensionless parameters Kn_R and Kn_N emerged in Eq. (13) are the two important Knudsen numbers reflecting the regime of phonon transport dynamics and the properties of heat conduction. A map of four different phonon transport regimes are quantitatively described by different values of Knudsen numbers [16, 47, 48, 49]:

(a) Ballistic regime: $Kn_R \gg 1, Kn_N \gg 1$. The ballistic regime happens when the characteristic length of the system is comparable to or smaller than the phonon mean free path. In this regime, the phonon transport is blocked by boundary scatterings so that the thermal conductivity decreases significantly as the system size shrinks [50, 7].

(b) Diffusive regime: $Kn_R \ll 1$. The diffusive regime is the most commonly encountered regime, where the resistive scattering is very strong. In this regime, the Fourier's law of heat conduction is valid.

(c) Hydrodynamic regime: $Kn_N \ll 1 \ll Kn_R$. The phonon hydrodynamic regime happens when the normal scattering dominates the heat conduction, i.e., in extremely low temperature or low-dimensional materials. In this regime, the normal scattering is much stronger than the boundary scattering, while the boundary scattering is much stronger than the resistive scattering [3, 51].

3. Iterative Schemes

3.1. Algorithms

The steady state solution of Eq. (13) is usually solved by the CIS: given its value at the n-th iteration step, the distribution function at the next iteration step is resolved from

$$\boldsymbol{v} \cdot \frac{\partial e^{n+1}}{\partial \boldsymbol{x}} = \frac{e_{eq}^{R,n} - e^{n+1}}{Kn_R} + \frac{e_{eq}^{N,n} - e^{n+1}}{Kn_N}, \qquad (16)$$

where the spatial derivative is approximated, in this work, by the second-order upwind finite difference scheme (degrades to the first-order upwind scheme in the layer at boundaries) or the discontinuous Galerkin method. The equilibrium distribution functions $e_{eq}^{R,n}$ and $e_{eq}^{N,n}$ are calculated by the corresponding macroscopic quantities, say $\boldsymbol{M}^n = [T^n, \boldsymbol{q}^n]^\top$ (the superscript '$\top$' is the transpose operator), which are obtained from e^n at the n-th iteration step according to Eq. (15). The boundary condition is also determined from e^n if necessary. Once e^{n+1} is obtained, we update the macroscopic quantities to $\boldsymbol{M}^{n+1}$. The iteration terminates when the relative error in the macroscopic quantities between two consecutive iterations are less than a preassigned value. The CIS is efficient when Kn_R and Kn_N are not small, where the converged solutions can be obtained within a few iterations. However, the total number of iteration needed has a sharp increase when either Kn_R or Kn_N becomes small.

To expedite the convergence, that is, to reduce the number of iteration steps, the GSIS is proposed. The key ingredient is that macroscopic synthetic equations are simultaneously solved with the transport equation to guide the evolution of the macroscopic quantities and

the distribution function. The synthetic equations are designed as follows. On multiplying Eq. (13) by 1, v_i, $v_i v_j$, respectively, where $i, j = 1, 2, 3$ represent the three orthogonal directions of the Cartesian coordinates and integrating the resultant equations with respect to the solid angle Ω, we obtain the following moments equations for temperature and heat flux (the Einstein summation convention is used)

$$\frac{\partial q_k}{\partial x_k} = 0, \tag{17}$$

$$\frac{1}{3}\frac{\partial T}{\partial x_i} + \frac{\partial N_{\langle ik \rangle}}{\partial x_k} = -\frac{1}{Kn_R}q_i, \tag{18}$$

$$\frac{2}{5}\frac{\partial q_{\langle i}}{\partial x_{j \rangle}} + \frac{\partial M_{\langle ijk \rangle}}{\partial x_k} = -\frac{1}{Kn_C}N_{\langle ij \rangle}, \tag{19}$$

where $Kn_C^{-1} = Kn_R^{-1} + Kn_N^{-1}$ is the overall Knudsen number and

$$\frac{\partial q_{\langle i}}{\partial x_{j \rangle}} = \frac{1}{2}\frac{\partial q_i}{\partial x_j} + \frac{1}{2}\frac{\partial q_j}{\partial x_i} - \frac{1}{3}\frac{\partial q_k}{\partial x_k}\delta_{ij}, \tag{20}$$

with δ being the Kronecker function. The definition of the moments $N_{\langle ik \rangle}$ and $M_{\langle ijk \rangle}$ reads

$$N_{\langle ik \rangle} = \int \left(v_i v_k - \frac{1}{3}\delta_{ik} \right) e \, d\Omega, \tag{21}$$

$$M_{\langle ijk \rangle} = \int v_i v_j v_k e \, d\Omega - \frac{1}{5}\int (v_i \delta_{jk} + v_j \delta_{ik} + v_k \delta_{ij}) e \, d\Omega, \tag{22}$$

which are symmetry and trace-free tensors [20]. Note that on deriving Eqs. (17) and (18), the fact that energy is conserved in both the normal and resistive scatterings and momentum is conserved in normal scattering has been applied.

The moment equations are not closed because the equation (19) for $N_{\langle ij \rangle}$ contains the high-order moments $M_{\langle ijk \rangle}$ that is unknown in terms of the lower-order moments. Fryer and Struchtrup [20] closed the equations by Grad's moment method, where the distribution function is truncated and approximated by a limited number of moments based on the principle of maximum entropy. If T, q_i and $N_{\langle ij \rangle}$ are chosen as the variables, $M_{\langle ijk \rangle}$ vanishes and the above momentum equations are reduced to the Guyer-Krumhansl equations. If $M_{\langle ijk \rangle}$ is also considered as the variables, additional constitutive relation is formulated for $M_{\langle ijk \rangle}$, resulting in the 16-Moment equations. However, with the truncation on the high-order moments, the Grad's moment equations are only valid in regimes of modest Knudsen numbers. Since we are considering phonon transport over the whole range of Knudsen numbers, we will close the equations (17)-(19) by calculating $M_{\langle ijk \rangle}$ with respect to the definition (22), using the solution of the distribution function from the Boltzmann equation. In this way, all the ballistic effects are included in $M_{\langle ijk \rangle}$ and no truncation is introduced. Details of implementation are described below.

After obtaining the macroscopic synthetic equations, we elaborate the procedure of the GSIS. Given the distribution function e^n and the macroscopic quantities $\boldsymbol{M}^n$ at the n-th iteration step, their values at the next steps $(n+1)$-th are updated as follows:

1. An intermediate solution of the distribution function at $(n + 1/2)$-th step is first obtained by solving the phonon transport equation

$$\boldsymbol{v} \cdot \frac{\partial e^{n+1/2}}{\partial \boldsymbol{x}} = \frac{e_{eq}^{R,n} - e^{n+1/2}}{Kn_R} + \frac{e_{eq}^{N,n} - e^{n+1/2}}{Kn_N}, \tag{23}$$

   where the equilibrium $e_{eq}^{R,n}$ and $e_{eq}^{N,n}$ are evaluated from $\boldsymbol{M}^n$ and the boundary condition is determined based on e^n;

2. The intermediate $e^{n+1/2}$ is then used to evaluated the high-order moment $M_{\langle ijk \rangle}^{n+1/2}$ and the macroscopic quantities $\boldsymbol{M}^{n+1/2}$ at boundaries according to Eqs. (22) and (15);

3. Provided the high-order moment and boundary condition, the macroscopic quantities M^{n+1} are resolved from the synthetic equations

$$\frac{\partial q_k^{n+1}}{\partial x_k} = 0,$$

$$\frac{1}{3}\frac{\partial T^{n+1}}{\partial x_i} + \frac{1}{Kn_R}q_i^{n+1} + \frac{\partial N_{\langle ik \rangle}^{n+1}}{\partial x_k} = 0, \tag{24}$$

$$\frac{1}{Kn_C}N_{\langle ij \rangle}^{n+1} + \frac{2}{5}\frac{\partial q_{\langle i}^{n+1}}{\partial x_{j \rangle}} = -\frac{\partial M_{\langle ijk \rangle}^{n+1/2}}{\partial x_k},$$

   which will be further used to calculate the equilibrium distributions in Eq. (23) in the next round of iteration;

4. The distribution function is simply updated as $e^{n+1} = e^{n+1/2}$.

The above steps are repeated until the difference between $\boldsymbol{M}^n$ and $\boldsymbol{M}^{n+1}$ is less than a small value. In this way, the GSIS can achieve fast convergence as the macroscopic equations allows very efficient propagation of information and the steady state can be quickly achieved. The implementations of both the CIS and GSIS are sketched in Fig. 1.

3.2. Fourier stability analysis

In this section, we adopt the Fourier stability analysis to rigorously calculate the convergence rates of both the CIS and GSIS in systems with periodic boundary conditions, that is, to see how fast the error decays as the iteration is carried forward.

We first consider the CIS and define the error function between the distribution functions at two consecutive iterations as [52]

$$Y^{n+1}(\boldsymbol{x}, \boldsymbol{s}) = e^{n+1}(\boldsymbol{x}, \boldsymbol{s}) - e^n(\boldsymbol{x}, \boldsymbol{s}), \tag{25}$$

and the error functions for the macroscopic quantities $\boldsymbol{M} = [T, \boldsymbol{q}]^\top$ between two consecutive iteration steps as

$$\begin{aligned}\boldsymbol{\Phi}_{\boldsymbol{M}}^{n+1}(\boldsymbol{x}) &\equiv \left[\Phi_T^{n+1}(\boldsymbol{x}), \boldsymbol{\Phi}_{\boldsymbol{q}}^{n+1}(\boldsymbol{x})\right]^\top \\ &= \boldsymbol{M}^{n+1}(\boldsymbol{x}) - \boldsymbol{M}^n(\boldsymbol{x}) = \int Y^{n+1}(\boldsymbol{x}, \boldsymbol{s})\boldsymbol{\phi}(\boldsymbol{v})\mathrm{d}\Omega,\end{aligned} \tag{26}$$
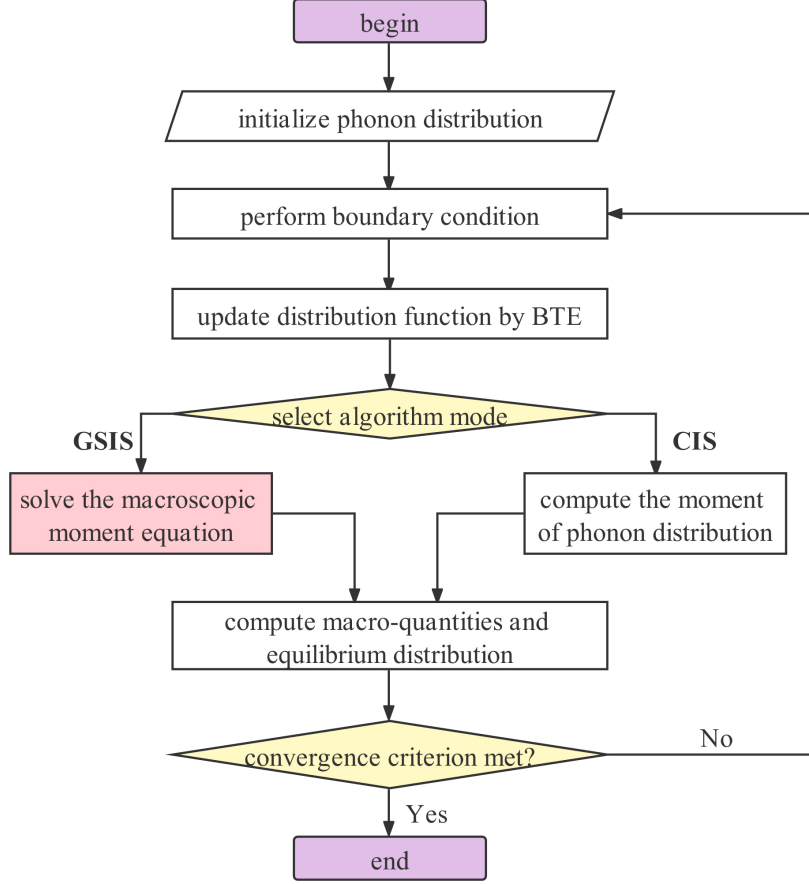
Figure 1: Schematic of procedures for CIS and GSIS. Generally, both the schemes follow similar solution routines. The major difference lies in the way to update macro quantities. In CIS, the macro quantities at new iteration step is calculated by taking moments of the distribution function. In GSIS, the macro quantities are obtained by solving the macroscopic synthetic equations.

where $\boldsymbol{\phi}(\boldsymbol{v}) = [1, \boldsymbol{v}]$. On substituting Eqs. (25) and (26) into Eq. (16), it is found that $Y^{n+1}(\boldsymbol{x}, \boldsymbol{s})$ satisfies

$$\boldsymbol{v} \cdot \boldsymbol{\nabla} Y^{n+1} + \frac{1}{Kn_C} Y^{n+1} = \frac{1}{4\pi Kn_C} \Phi_T^n + \frac{3}{4\pi Kn_N} \boldsymbol{v} \cdot \boldsymbol{\Phi_q^n}. \tag{27}$$

To determine the convergence rate, we perform the Fourier stability analysis and express the error functions as

$$Y^{n+1}(\boldsymbol{x}, \boldsymbol{s}) = y^{n+1}(\boldsymbol{s}) \exp(\mathbf{i}\boldsymbol{\theta} \cdot \boldsymbol{x}), \tag{28}$$

$$\boldsymbol{\Phi}_M^{n+1}(\boldsymbol{x}) = \boldsymbol{\alpha}_M^{n+1} \exp(\mathbf{i}\boldsymbol{\theta} \cdot \boldsymbol{x}), \tag{29}$$

where $\boldsymbol{\theta} = (\theta_1, \theta_2, \theta_3)$ is the wavevector of perturbation, $\mathbf{i}$ is the imaginary unit, and y^{n+1} and $\boldsymbol{\alpha}_M^{n+1} = \left[\boldsymbol{\alpha}_T^{n+1}, \boldsymbol{\alpha}_q^{n+1}\right]^\top$ are the Fourier expansion coefficients. Substituting Eq. (28) and (29) into Eq. (27), we obtain the relation between y and $\boldsymbol{\alpha}_M$ as

$$(1 + \mathbf{i}Kn_C \boldsymbol{v} \cdot \boldsymbol{\theta}) \, y^{n+1} = \frac{1}{4\pi} \alpha_T^n + \frac{3Kn_C}{4\pi Kn_N} \boldsymbol{v} \cdot \boldsymbol{\alpha}_q^n. \tag{30}$$

10

Note that we only consider the single Fourier mode $\exp(\mathtt{i}\boldsymbol{\theta}\cdot\boldsymbol{x})$ because Eq. (27) is a linear system, and all the other modes independently follows the same relation of (30). For simplification, we consider general two-dimensional problem and set $\theta_3 = 0$ without losing essential properties of the error evolution. We further constrain that $|\boldsymbol{\theta}|^2 = \theta_1^2 + \theta_2^2 = 1$. Although the actual perturbation may have various values of $|\boldsymbol{\theta}|$, from Eq. (30) we can see that y^{n+1} depends on $\boldsymbol{\theta}$ through the product $Kn_C\boldsymbol{\theta}$. For cases $|\theta| \neq 1$, the convergence rate can be obtained by replacing Kn_C with $Kn_C|\theta|$ and keeping the ratio Kn_C/Kn_N unchanged.

On introducing Eqs. (28), (29) and (30) into Eq. (26), we have

$$\boldsymbol{\alpha}_M^{n+1} = \mathbf{C}\boldsymbol{\alpha}_M^n, \tag{31}$$

where the 3×3 matrix $\mathbf{C}$ is

$$\mathbf{C} = \begin{bmatrix} c_1 \int y'\mathrm{d}\Omega & c_2 \int v_1 y'\mathrm{d}\Omega & c_2 \int v_2 y'\mathrm{d}\Omega \\ c_1 \int v_1 y'\mathrm{d}\Omega & c_2 \int v_1^2 y'\mathrm{d}\Omega & c_2 \int v_1 v_2 y'\mathrm{d}\Omega \\ c_1 \int v_2 y'\mathrm{d}\Omega & c_2 \int v_1 v_2 y'\mathrm{d}\Omega & c_2 \int v_2^2 y'\mathrm{d}\Omega \end{bmatrix}, \tag{32}$$

with

$$c_1 = \frac{1}{4\pi}, \quad c_2 = \frac{3Kn_C}{4\pi Kn_N}, \quad y' = \frac{1}{1 + \mathtt{i}Kn_C\boldsymbol{v}\cdot\boldsymbol{\theta}}. \tag{33}$$

Eq. (31) allows us to determine the errors of the macroscopic quantities recursively

$$\boldsymbol{\Phi}_M^{n+1} = \mathbf{C}\boldsymbol{\Phi}_M^n = \cdots = \mathbf{C}^n\boldsymbol{\Phi}_M^1. \tag{34}$$

Given an initial guess of the macroscopic quantities $\boldsymbol{M}^0$, this yields the estimation

$$\frac{\|\boldsymbol{\Phi}_M^{n+1}\|}{\|\boldsymbol{\Phi}_M^1\|} = \frac{\|\boldsymbol{M}^{n+1} - \boldsymbol{M}^n\|}{\|\boldsymbol{M}^1 - \boldsymbol{M}^0\|} \leq \|\mathbf{C}^n\| \simeq \rho^n. \tag{35}$$

Here ρ is the magnitude of the largest eigenvalue of the matrix $\mathbf{C}$, i.e., the convergence rate. Eq. (35) implies: when $\rho > 1$, the iteration is unstable; when $\rho < 1$ the iteration converges, however the convergence is very slow if $\rho \simeq 1$; and the iteration can efficiently suppress the error when $\rho \simeq 0$.

The convergence rate ρ can be obtained by numerically computing the eigenvalues of the matrix $\mathbf{C}$ and taking the maximum absolute value. The results as a function of Kn_R and Kn_N are shown in the left plot of Figure 2. It is clear that when both Kn_R and Kn_N are large, ρ goes to zero so that the error decays quickly. That is the CIS is quite efficient in the ballistic regime. However, when either Kn_R or Kn_N is small, the convergence rate ρ is close to 1, which indicates that the CIS works inefficiently such that it requires large numbers of iteration steps for convergence in the diffusive, hydrodynamic, and Ziman regimes.

To evaluate the convergence rate of the GSIS, the error function for the distribution function is modified as

$$Y^{n+1/2}(\boldsymbol{x}, \boldsymbol{s}) = e^{n+1/2}(\boldsymbol{x}, \boldsymbol{s}) - e^n(\boldsymbol{x}, \boldsymbol{s}) = y^{n+1/2}(\boldsymbol{s})\exp(\mathtt{i}\boldsymbol{\theta}\cdot\boldsymbol{x}). \tag{36}$$

According to Eq. (23), $y^{n+1/2}$ has the same solution (30) as that for y^{n+1} in the CIS. The error functions of the macroscopic quantities are still defined as $\boldsymbol{\Phi}_M^{n+1} = \boldsymbol{M}^{n+1} - \boldsymbol{M}^n$. However, unlike the CIS where $\boldsymbol{\Phi}_M^{n+1}$ are directly calculated as the integrals of the error function for the distribution function, in the GSIS they are obtained from the macroscopic synthetic equations (24), in which T^{n+1} and $\boldsymbol{q}^{n+1}$ are replaced by Φ_T^{n+1} and $\boldsymbol{\Phi}_{\boldsymbol{q}}^{n+1}$, $N_{\langle ij \rangle}^{n+1}$ are replaced by

$$\Phi_{N_{\langle ij \rangle}}^{n+1} \equiv N_{\langle ij \rangle}^{n+1} - N_{\langle ij \rangle}^n = \alpha_{N_{\langle ij \rangle}}^{n+1} \exp(\mathrm{i}\boldsymbol{\theta} \cdot \boldsymbol{x}), \tag{37}$$

and $M_{\langle ijk \rangle}$ are replaced by

$$\Phi_{M_{\langle ijk \rangle}}^{n+1/2} \equiv \int v_i v_j v_k Y^{n+1/2} \mathrm{d}\Omega - \frac{1}{5} \int (v_i \delta_{jk} + v_j \delta_{ik} + v_k \delta_{ij}) Y^{n+1/2} \mathrm{d}\Omega, \tag{38}$$

because only the highest-order moment $M_{\langle ijk \rangle}$ is calculated from the distribution function when solving the synthetic equations. After some simple algebraic calculates we have

$$\mathrm{i}\theta_k \alpha_{q_k}^{n+1} = 0,$$

$$\frac{1}{3}\mathrm{i}\theta_i \alpha_T^{n+1} + \frac{1}{Kn_R} \alpha_{q_i}^{n+1} + \mathrm{i}\theta_k \alpha_{N_{\langle ik \rangle}}^{n+1} = 0,$$

$$\frac{1}{Kn_C} \alpha_{N_{\langle ij \rangle}}^{n+1} + \frac{1}{5}\mathrm{i}\theta_j \alpha_{q_i}^{n+1} + \frac{1}{5}\mathrm{i}\theta_i \alpha_{q_j}^{n+1} = -\mathrm{i}\theta_k \int v_i v_j v_k y^{n+1/2} \mathrm{d}\Omega \tag{39}$$

$$+ \frac{1}{5}\mathrm{i}\theta_k \int (v_i \delta_{jk} + v_j \delta_{ik} + v_k \delta_{ij}) y^{n+1/2} \mathrm{d}\Omega.$$

On eliminating $\alpha_{N_{\langle ij \rangle}}^{n+1}$ and replacing $y^{n+1/2}$ by its solution, we eventually obtain the following 3×3 linear systems for general two-dimensional problems

$$\mathbf{L}\boldsymbol{\alpha}_M^{n+1} = \mathbf{R}\boldsymbol{\alpha}_M^n, \tag{40}$$

where

$$\mathbf{L} = \begin{pmatrix} 0 & \mathrm{i}\theta_1 & \mathrm{i}\theta_2 \\ \frac{1}{3}\mathrm{i}\theta_1 & \frac{2Kn_C}{5}\theta_1^2 + \frac{Kn_C}{5}\theta_2^2 + \frac{1}{Kn_R} & \frac{Kn_C}{5}\theta_1\theta_2 \\ \frac{1}{3}\mathrm{i}\theta_2 & \frac{Kn_C}{5}\theta_1\theta_2 & \frac{Kn_C}{5}\theta_1^2 + \frac{2Kn_C}{5}\theta_2^2 + \frac{1}{Kn_R} \end{pmatrix},$$

$$\mathbf{R} = \begin{pmatrix} 0 & 0 & 0 \\ c_1 \int s_1 y' \mathrm{d}\Omega & c_2 \int v_1 s_1 y' \mathrm{d}\Omega & c_2 \int v_2 s_1 y' \mathrm{d}\Omega \\ c_1 \int s_2 y' \mathrm{d}\Omega & c_2 \int v_1 s_2 y' \mathrm{d}\Omega & c_2 \int v_2 s_2 y' \mathrm{d}\Omega \end{pmatrix}, \tag{41}$$

with

$$s_1 = -Kn_C \left[\theta_1^2 \left(v_1^2 - \frac{2}{5} \right) v_1 + \theta_1\theta_2 v_1^2 v_2 + \theta_1\theta_2 \left(v_1^2 - \frac{1}{5} \right) v_2 + \theta_2^2 \left(v_2^2 - \frac{1}{5} \right) v_1 \right],$$

$$s_2 = -Kn_C \left[\theta_1^2 \left(v_1^2 - \frac{1}{5} \right) v_2 + \theta_1\theta_2 \left(v_2^2 - \frac{1}{5} \right) v_1 + \theta_1\theta_2 v_1 v_2^2 + \theta_2^2 \left(v_2^2 - \frac{2}{5} \right) v_2 \right]. \tag{42}$$

Consequently, the convergence rate of the GSIS is calculated as the magnitude of the maximum eigenvalue of the matrix $\mathbf{G} = \mathbf{L}^{-1}\mathbf{R}$. The results are shown in the right plot of
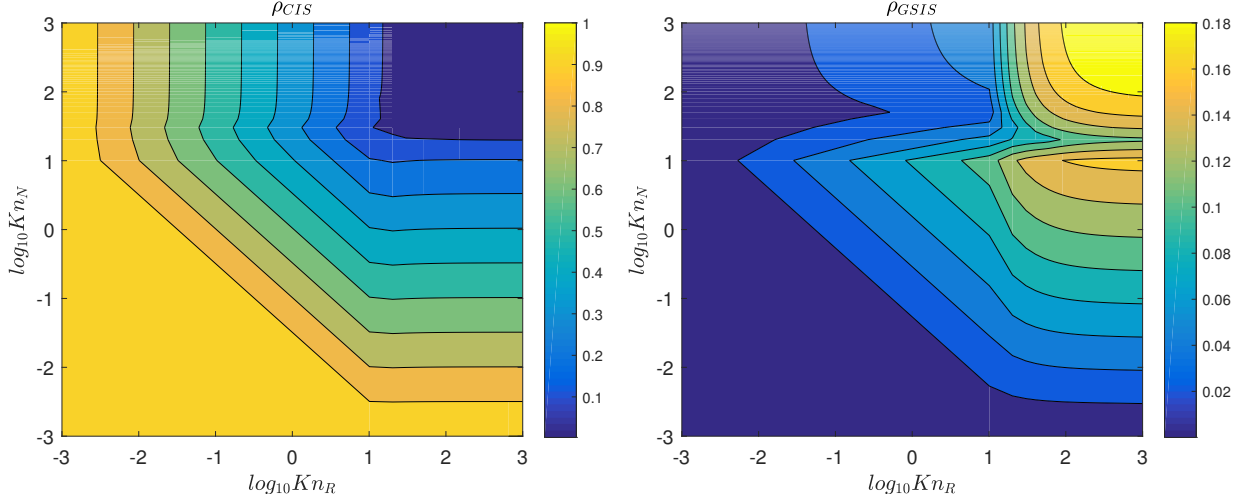
Figure 2: The contours of convergence rate ρ as a function of the Knudsen numbers Kn_R and Kn_N (in logarithmic scales) from 10^{-3} to 10^3 for both the CIS (Left) and the GSIS (Right). The results are obtained considering general two-dimensional problems when the wavevector of perturbations is set as $\boldsymbol{\theta} = (1/\sqrt{2}, 1/\sqrt{2})$.

Figure 2. It is clearly illustrated that compared to the CIS, the GSIS greatly improves the iteration efficiency especially in regimes of small values of Kn_R and Kn_N. The convergence rate can always be maintained under 0.2, which means that only 2 iterations are required to reduce the iterative error by one order of magnitude.

Note that in Figure 2, the convergence rates are obtained when $(\theta_1, \theta_2) = \left(1/\sqrt{2}, 1/\sqrt{2}\right)$. It has been tested that different values of $\boldsymbol{\theta}$ make no difference in the results.

4. Numerical tests

In this section, we numerically demonstrate the performance of GSIS and CIS in three confined systems that can be treated as prototypes for real engineering applications.

4.1. Quasi one-dimensional heat conduction across an infinitely thin sheet

The quasi one-dimensional heat conduction across an infinitely thin sheet of length $L = 1$, as shown in Fig. 3(a), is simulated by both the CIS and the GSIS. The simulation domain is set as $x_1 \in [0, 1]$. Temperatures deviated from the reference temperature on the left and right boundaries are $T_H = 1/2$ and $T_C = -1/2$, respectively. The thermalization boundary condition is adopted for the distribution function of phonons interacted with the isothermal surface, where a phonon is absorbed as it strikes the boundary and a new phonon in the equilibrium state with the boundary temperature is emitted into the computational domain. Therefore, the distributions of the phonons reflected from the boundaries are

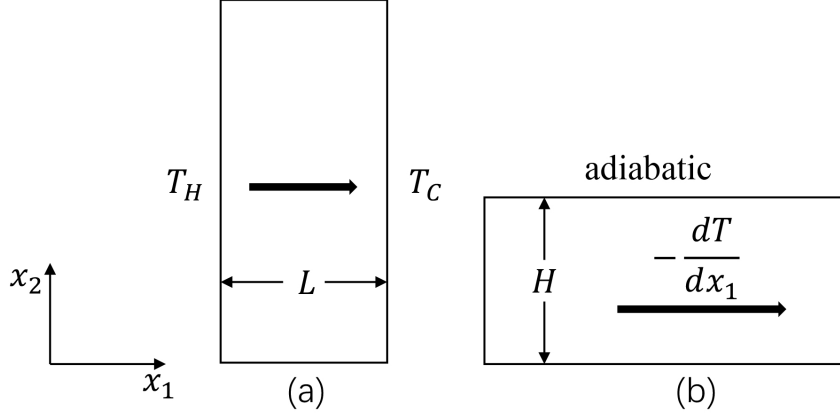$$e(x_1 = 0, v_1 > 0) = \frac{T_H}{4\pi}, \quad e(x_1 = 1, v_1 < 0) = \frac{T_C}{4\pi}. \tag{43}$$

Figure 3: Schematics of (a) quasi one-dimensional heat conduction in an infinitely thin sheet with a length L induced by the different temperatures of the left and right boundaries; (b) quasi one-dimensional heat conduction in a infinitely long film with a height H induced by a constant temperature gradient in its longitudinal direction. The boundaries at the transverse direction are adiabatic.

For this one-dimensional case, the moment equations can be simplified to $\partial q_1/\partial x_1 = 0$, i.e., the heat flux is a constant, while the temperature satisfies

$$\frac{Kn_R}{3}\frac{\partial T}{\partial x_1} - Kn_C Kn_R \frac{\partial^2}{\partial x_1^2} M_{111} = -q_1. \tag{44}$$

On integrating Eq. (44) with respect to x_1 over the domain and considering the symmetry around $x_1 = 1/2$, we obtain the solution at the $(n+1)$-th step as

$$T^{n+1} = \frac{3}{Kn_R} q_1^{n+1} \left(\frac{1}{2} - x_1 \right) + 3Kn_C \frac{\partial M_{111}^{n+1/2}}{\partial x_1}. \tag{45}$$

The constant heat flux is calculated from the temperature and high-order moment at the boundary as

$$q_1^{n+1} = \frac{2Kn_R}{3} T^{n+1/2} \bigg|_{x_1=0} - 2Kn_C Kn_R \frac{\partial M_{111}^{n+1/2}}{\partial x_1} \bigg|_{x_1=0}, \tag{46}$$

where $T^{n+1/2}|_{x_1=0}$ is the temperature at the boundary that are evaluated from the distribution function $e^{n+1/2}$.

For numerical simulation, the spatial domain is discretized by the following non-uniform grid nodes

$$x_1^d = d^3 \left(10 - 15d + 6d^2 \right), \quad d = (0, 1, ..., N_x - 1)/(N_x - 1), \tag{47}$$

and totally $N_x = 101$ are used. The spatial derivatives in the governing equations are approximated by the second-order finite difference method. The Gauss-Legendre quadrature is adopted for the numerical integration with respect to the solid angle Ω and 60 discrete points are used in the polar angle, i.e., $N_\theta = 60$. The iteration is assumed to converge when

$$\epsilon = \int_0^1 |T^{n+1} - T^n| \mathrm{d}x_1 < 1.0 \times 10^{-7}. \tag{48}$$
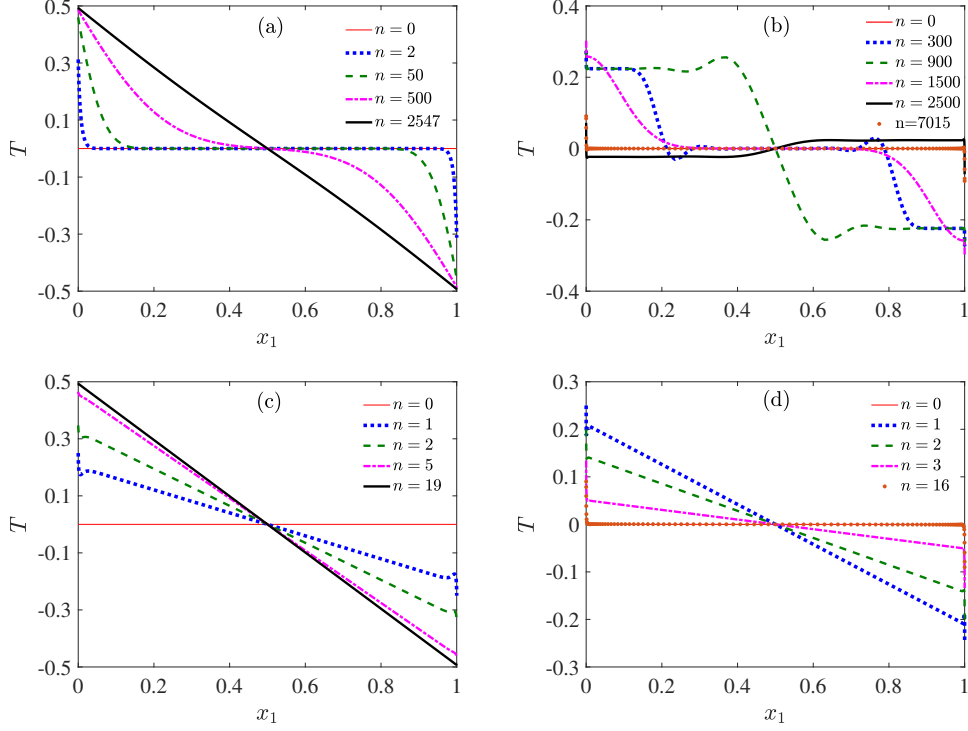
14

Figure 4: Immediate temperature profiles of quasi one-dimensional heat conduction in an infinitely thin sheet at different iteration steps obtained from CIS (a, b) and GSIS (c, d). In (a, c) $Kn_R = 10^{-2}, Kn_N = 10^5$, and in (b, d) $Kn_R = 10^5, Kn_N = 10^{-3}$.

To illustrate the convergence properties of the CIS and the GSIS, we compare the convergence histories of the two schemes in terms of the intermediate temperature profiles at selected iteration steps. The results when $Kn_R = 10^{-2}$ and $Kn_N = 10^5$, i.e., the phonon transport belongs to the diffusive regime, are plotted in Fig. 4(a) and (c). In the CIS, starting from the initial condition $T = 0$, the heat flux from the boundaries quickly changes the temperature locally (within about one phonon mean free path away from the boundaries); however, due to the frequent resistive scattering, it takes a large number of iteration steps for the perturbation to propagate into the bulk region. For example, from Fig. 4(a) we see that about 500 iteration steps are consumed for the temperature at $x = 0.5$ to feel this change; then it costs additional 2000 steps to adjust the temperature towards the final linear profile. Such a slow convergence is completely changed in the GSIS, where the temperature are updated according to the macroscopic equations (44), in which the dominated part is $\partial T / \partial x_1 = -3q_1/Kn_R$ when Kn_R is small and Kn_N is large. This implies that the temperature in the bulk region can be immediately corrected to be nearly linear, which is the major reason for the fast convergence of the GSIS. As we can see from Fig. 4(c), the temperature in the bulk region has perceived the perturbation from the boundaries just after 1 iteration and it varies linearly as the computation continues.

Now we consider the convergence property for the phonon transport in the hydrodynamic regime with $Kn_R = 10^5$ and $Kn_N = 10^{-3}$. For this case, due to the non-negligible effect of
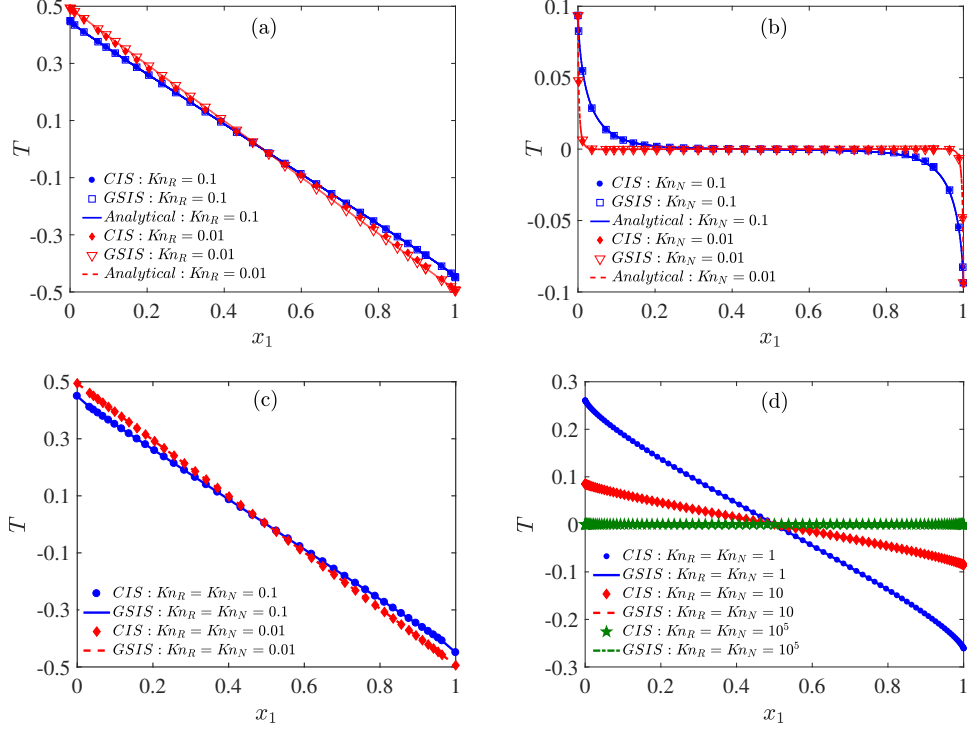
15

Figure 5: Steady-state temperature profiles of quasi one-dimensional heat conduction across an infinitely thin sheet. (a) Diffusive regime: $Kn_N = 10^5, Kn_R = 0.1, 0.01$; (b) phonon hydrodynamic regime: $Kn_R = 10^5, Kn_N = 0.1, 0.01$; (c) Ziman regime: $Kn_R = Kn_N = 0.1, Kn_R = Kn_N = 0.01$; (d) ballistic regime: $Kn_R = Kn_N = 1, Kn_R = Kn_N = 10, Kn_R = Kn_N = 10^5$.

high-order moments, the steady-state temperature has a profile that varies greatly near the boundaries but has almost zero value in the bulk region. The results from the CIS is plotted in Fig. 4(b). It is found that as the iteration processes, the perturbation from the boundaries first propagates into the bulk region, e.g., during the first 900 steps; then the effect from the high-order moments gradually manifests and it slowly regulates the temperature in the bulk region to the final state, which cost another several thousands of steps. The results from the GSIS is illustrated in Fig. 4(d), where the slow convergence, again, is changed. It is interesting to note that, the temperature is immediately aroused linearly in the bulk region after 1 iteration, just as that found in the previous case; this is due to the fact that the high-order terms are explicitly evaluated from the first solution of the distribution function, which is very close to zero especially in the bulk region; in other words, during (but only during) the first iteration, the macroscopic equations behave like the diffusion equation. However, after then, the high-order moment quickly becomes effective, and the temperature reaches the steady state within several iterations. Therefore, with the help of the macroscopic synthetic equations that allow very efficient exchange of information, the GSIS realizes fast convergence in the whole computational domain.

Figure 5 shows the temperatures predicted by the two schemes under various combinations of Kn_R and Kn_N. Results from the GSIS are in good agreements with the analytical

16

Table 1: Number of iteration steps cost by CIS and GSIS for converged solutions [Eq. (48)] for quasi one-dimensional heat conduction across an infinitely thin sheet.

Kn_R	10	1	0.1	0.01	10^5	10^5	10^5	10^5	10^5	0.01
Kn_N	10^5	10^5	10^5	10^5	10	1	0.1	0.01	0.001	0.01
CIS	4	9	83	2547	5	13	69	608	7015	4025
GSIS	5	8	17	19	6	11	14	15	16	19

solutions [45], therefore the accuracy of the GSIS is validated. Note that as fine enough spatial grid is used, the CIS results are also accurate. We record the total number of iterations needed for the convergence for the schemes in Table 1. It is found that the iteration numbers are significantly reduced by the GSIS when either of the Knudsen numbers is small. When both the Knudsen numbers are large, the two schemes costs almost the same number of iterations and both the schemes are efficient.

4.2. Quasi one-dimensional heat conduction in an infinitely long film

In this section, we consider a quasi one-dimensional heat transport in a infinitely long film having a height of $H = 1$, see Fig. 3(b). The simulation domain is $(x_1, x_2) \in [-0.5, 0.5]^2$. The periodic heat flux boundary condition is applied on both the left-hand and right-hand ends to preserve a constant temperature gradient along the longitudinal direction, while the other two boundaries are adiabatic. This implementation of boundary condition can model the heat transport in an infinitely long sample and avoid a large number of spatial grid cells along the longitudinal direction [53, 41]. The distribution function at the left and right boundaries are given as

$$
\begin{aligned}
e(x_1 = -0.5, x_2, v_1 > 0) &= \frac{\Delta T}{4\pi} + e(x_1 = -0.5, x_2, v_1 > 0), \\
e(x_1 = 0.5, x_2, v_1 < 0) &= -\frac{\Delta T}{4\pi} + e(x_1 = 0.5, x_2, v_1 < 0),
\end{aligned}
\tag{49}
$$

where $\Delta T = 1$ is the temperature difference between the two ends. Two kinds of numerical treatments are available for the adiabatic boundary: the specular scheme and the diffuse scheme. Due to material roughness, the diffuse scheme is often a better approximation, which assumes that the direction of phonon leaving from the boundary is independent of that of the incident phonon. We adopt the nonthermalizing diffuse scheme for the bottom and top boundaries to ensure accurate energy conservation [53]

$$
\begin{aligned}
e(x_1, x_2 = -0.5, v_2 > 0) &= -\frac{\int_{v_2<0} e(x_1, x_2 = -0.5) v_2 \mathrm{d}\Omega}{\int_{v_2>0} v_2 \mathrm{d}\Omega}, \\
e(x_1, x_2 = 0.5, v_2 < 0) &= -\frac{\int_{v_2>0} e(x_1, x_2 = 0.5) v_2 \mathrm{d}\Omega}{\int_{v_2<0} v_2 \mathrm{d}\Omega}.
\end{aligned}
\tag{50}
$$

For simulations, $N_{x_1} = 3$ equidistant spatial nodes are used for the x_1-direction, and $N_{x_2} = 101$ non-uniform nodes determined by Eq. (47) are employed in the x_2-direction. An angular
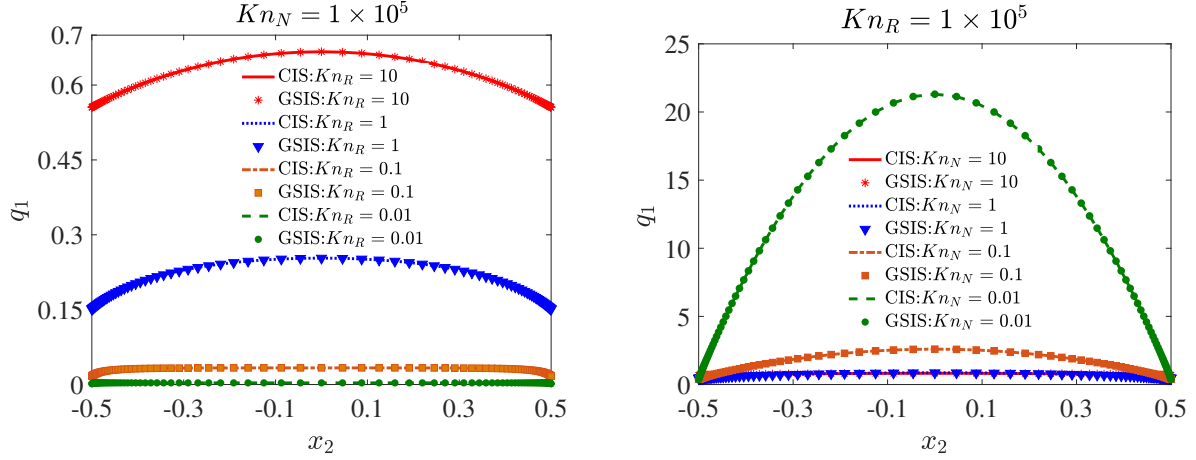
Figure 6: Steady-state heat flux along the transverse direction of quasi one-dimensional heat condition in an infinitely long film. (left) In the diffusive regime with $Kn_N = 10^5$ and different $Kn_R = 10, 1, 0.1, 0.01$; (right) in the hydrodynamic regime with $Kn_R = 10^5$ and different $Kn_N = 10, 1, 0.1, 0.01$.

Table 2: Number of iteration steps n cost by CIS and GSIS for converged solutions [Eq. (51)] for quasi one-dimensional heat conduction in an infinitely long film.

Kn_R	10	1	0.1	0.01	10^5	10^5	10^5	10^5	10^5
Kn_N	10^5	10^5	10^5	10^5	10	1	0.1	0.01	0.001
CIS	81	22	37	43	87	64	892	54614	-
GSIS	81	22	32	30	8	39	35	60	68

resolution of $N_\theta = 24$, $N_\varphi = 24$ are adopted. The convergence criterion is

$$\epsilon = \int_{-0.5}^{0.5} |T^{n+1}(x_1 = 0, x_2) - T^n(x_1 = 0, x_2)| \mathrm{d}x_2 < 1.0 \times 10^{-7}. \tag{51}$$

Figure 6 shows the steady-state heat flux along the x_2 direction in the diffusive and hydrodynamic regimes obtained by both the CIS and GSIS under different combinations of Knudsen numbers. Again, the two schemes predict almost the same results. The numbers of iteration steps needed for converged solutions are listed in Table 2 for both the schemes. For all the cases when either Kn_R or Kn_N is small, the GSIS costs much fewer iterations to obtain the steady-state solutions. For example, when $Kn_N = 0.01$ and $Kn_R = 10^5$, the total iteration number for the CIS is 54614, while the GSIS only takes 60 iteration steps, thus the total number of iterations is nearly reduced by 3 orders of magnitude in the GSIS.

4.3. Quasi two-dimensional heat conduction in a square domain

Now we consider the heat conduction within a quasi two-dimensional square domain of dimensions $[0, 1] \times [0, 1]$. The upper boundary of the square is maintained at a higher temperature $T_H = 1$, and that of the other three boundaries is $T_C = 0$. We first consider four groups of Knudsen numbers to compare the temperature contours obtained from the GSIS and the CIS: $Kn_R = 0.01$, $Kn_N = 10^5$; $Kn_R = 0.1$, $Kn_N = 10^5$; $Kn_R = 1$, $Kn_N = 1$;
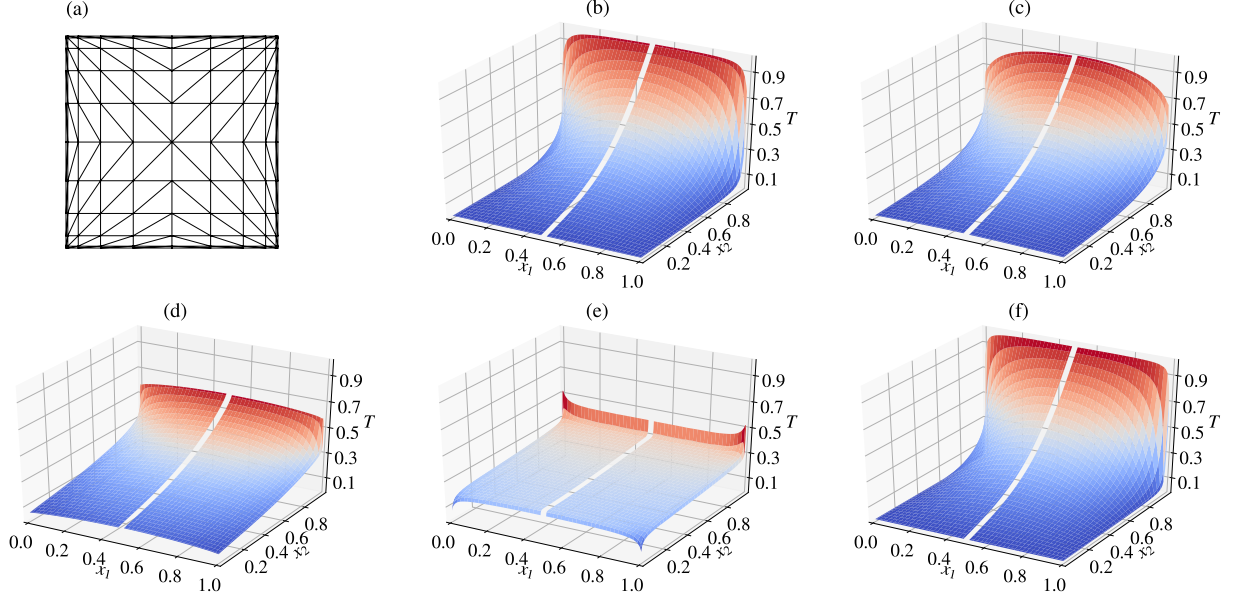
18

Figure 7: Heat conduction in quasi two-dimensional square domain. (a) Triangular mesh used to partition the domain. Temperature contours: (b) $Kn_R = 0.01$, $Kn_N = 10^5$, (c) $Kn_R = 0.1$, $Kn_N = 10^5$, (d) $Kn_R = 1$, $Kn_N = 1$, (e) $Kn_R = 10$, $Kn_N = 0.01$ and (f) $Kn_R = 0.001$, $Kn_N = 10^5$, where the right half domain in each subplot illustrates the result obtained from GSIS. In (b)-(e), the left half domain shows the result obtained from CIS. The left domain in (f) is the analytical solution obeying the Fourier's conduction law.

and $Kn_R = 10$, $Kn_N = 0.01$. The problem is simulated on the triangular mesh as illustrated in Figure 7. The mesh is generated in the following way: first 10 seeds are distributed along the x_1 and x_2 directions according to Eq. (47) to partition the domain into 10×10 rectangles; then each rectangle is split into two uniform triangles by connecting one pair of its across corners. This results in a mesh with totally 200 triangles and the maximum (minimum) cell size, i.e., the triangular height is about 0.13 (6.1×10^{-3}). The 4th-order discontinuous Galerkin finite element method is employed to discretize the kinetic equation as well as the moment equations in the spatial space. The detailed formulations can be found in the Appendix. An angular resolution of $N_\theta = 40$ and $N_\varphi = 80$ is adopted, except for the case of $Kn_R = 1$, $Kn_N = 1$ where we set $N_\theta = 80$ and $N_\varphi = 160$ to get a smooth solution. For all the calculations, both the GSIS and CIS iterations are terminated when

$$\epsilon = \sqrt{\frac{\int |T^{n+1} - T^n|^2 \mathrm{d}x_1 \mathrm{d}x_2}{\int |T^n|^2 \mathrm{d}x_1 \mathrm{d}x_2}} < 1.0^{-7}. \tag{52}$$

For the GSIS, the macroscopic quantities at the $(n+1)$-th step are updated as

$$\boldsymbol{M}^{n+1} = \beta \boldsymbol{M}^* + (1 - \beta) \boldsymbol{M}^e, \tag{53}$$

where $\boldsymbol{M}^*$ denotes the solution from the synthetic equations, and $\boldsymbol{M}^e$ are evalued from the solution e^{n+1} according to (11). The limiter β is defined as

$$\beta = \frac{\min\left(Kn_R/H_l, Kn_{th}\right)}{Kn_R/H_l}, \tag{54}$$

19

where H_l is the height of a local triangle that characterizes the local cell size; Kn_{th} is a preassigned threshold value that is set as $Kn_{th} = 100$ when $Kn_R = 10$, and $Kn_{th} = 1$ otherwise. This implementation is introduced to retain numerical stability, due the fact that the high-order terms become vary large when the local nonequilibrium effect near the solid corners is significant and the macroscopic equations become stiff.

The four boundaries of the domain are modeled as isothermal surfaces with the given temperatures. Thus, when solving the kinetic equation, the distributions of the phonon reflected from the boundaries are determined as

$$e\left(x_2 = 1, \boldsymbol{v} \cdot \boldsymbol{n} > 0\right) = \frac{T_H}{4\pi}, \quad e\left(x_1 = 0, 1 \text{ or } x_2 = 0, \boldsymbol{v} \cdot \boldsymbol{n} > 0\right) = \frac{T_C}{4\pi}, \tag{55}$$

where $\boldsymbol{n}$ denotes the unit normal vector of the boundaries pointing into the domain. For the moment equations, we impose the boundary condition in the following ways. The system is similar as the Stokes equations for fluid, if T and $\boldsymbol{q}$ are analog to the pressure and velocity vector of the Stokes flow. Therefore, the isothermal boundary condition can be implemented as the same as the pressure inlet condition for the Stokes equations [54]: the given temperature is imposed on the Neumann boundary by a pseudo-traction vector; while the heat flux at the boundary is obtained as part of the solution. However, when the conduction occurs in the phonon hydrodynamic regime with $Kn_R = 10$ and $Kn_N = 0.01$, the Neumann condition may lead to complete wrong solutions, because the rapid change of temperature in the vicinity of boundaries can result in a significant overestimation of heat flux. Then for this case, we specific the values of heat flux at the boundaries just as the Dirichlet condition for Stokes flows. All the boundary values of temperature and heat flux are calculated from $e^{n+1/2}$ to ensure correct temperature jump.

Figure 7(b)-(e) compare the temperature contours predicted by the GSIS (shown on the right half domain) and the CIS (shown on the left half domain). The two schemes obtain almost the same results in different phonon transport regimes. The numbers of iterative steps and the CPU time cost by each schemes are list in Table 3. The convergence property is coincident with that found in the previous sections for the one-dimensional problems: the GSIS can find the steady state solutions within several dozens of iterations for all the groups of Kn_R and Kn_N; when any of Kn_R and Kn_N is small, the GSIS can significantly reduce the iteration steps, compared to the CIS. Since the additional time used to solve the moment equations is much smaller than that for the kinetic equation, the saving of CPU time by the GSIS is proportional to the number of iterations it reduces, hence the GSIS can be much faster than the CIS.

Finally we push the simulation towards the Fourier conduction limit to check if the GSIS can recover the solution predicted by the Fourier's conduction law on such coarse mesh with the cell size much larger than the phonon mean free path. To this end, we set $Kn_R = 0.001$, $Kn_N = 10^5$, so the maximum (minimum) cell size is more than 100 (about 6) times of the mean free path. The Fourier's solution is determined by the Laplace equation $\nabla^2 T = 0$ as

$$\frac{T - T_C}{T_H - T_C} = \frac{2}{\pi} \sum_{m=1}^{\infty} \frac{(-1)^{m+1} + 1}{m} \sin\left(m\pi x_1\right) \frac{\sinh\left(m\pi x_2\right)}{\sinh\left(m\pi\right)}. \tag{56}$$

Table 3: Number of iteration steps n and CPU time cost by GSIS and CIS for converged solutions [Eq. (52)] for quasi two-dimensional condition problem under different combinations of Kn_R and Kn_N. N_{el} is the number of triangles of spatial meshes, N_θ and N_φ are the numbers of discrete points for angular resoltions. CPU time is counted by running each case on single Intel Xeon-E5-2680 processor.

case		N_{el}	N_θ	N_φ	GSIS		CIS	
Kn_R	Kn_N				n	CPU time [s]	n	CPU time [s]
0.001	10^5	200	20	40	43	23.6	-	-
0.01	10^5	200	40	80	24	54.2	13234	28938.5
0.1	10^5	200	40	80	26	59.3	269	587.2
1	1	200	80	160	28	260.4	29	255.5
10	0.01	200	40	80	47	106.9	1883	4112.2

In Figure 7(f), the right half domain plots the temperature contours obtained form the GSIS (terminated at the 44th iteration when $\epsilon < 10^{-7}$), while the analytical solution (56) is illustrated in the left half domain. It is found that the two results are in good agreement. Therefore, the GSIS can recover the Fourier's limit. For this problem, the CIS hardly gets a solution due to slow convergence, where the convergence rate is nearly 1.

5. Conclusions and outlooks

We have developed the general synthetic iterative scheme to expedite the convergence of the conventional iterative scheme in finding steady-state solutions for multiscale phonon transport problems that are described by Callaway's dual-relaxation model. The critical ingredient of the new scheme is that a set of macroscopic moment equations is tightly coupled and simultaneously solved with the Boltzmann transport equation. The synthetic macroscopic equations are strictly derived from the Boltzmann transport equation, which contain not only the diffusive/hydrodynamic part but also the high-order moments taking account all the nonequilibrium transport effects. During the iteration, macroscopic quantities such as temperature and heat flux are resolved from the macroscopic equations, which are used to calculate the equilibria in the scattering terms and guide the evolution of the phonon distribution function; meanwhile, the distribution function obtained from the Boltzmann transport equation provides the highest-order moments for the closure of the macroscopic synthetic equations. Since the macroscopic equations allows very efficient exchange of information over the whole computational domain, fast convergence in the entire range of Knudsen numbers is realized.

The Fourier stability analysis has been conducted for systems with periodic boundary conditions. The convergence rates of the two schemes have been rigorously calculated, thus the superiority of the new scheme over the conventional one has been revealed. It has been shown that the convergence rate of the GSIS can always be maintained under 0.2, so that only 2 iterations are required to reduce the iterative error by one order of magnitude. Several numerical tests in different phonon transport regimes further demonstrate the efficiency of the GSIS, especially in the diffusive and hydrodynamics regimes, where the number of

iteration steps as well as the CPU time are reduced by up to three orders of magnitude in the GSIS, compared to the conventional scheme.

For future works, we will extend the GSIS to nonlinear systems and multi-frequency model, and also consider unsteady-state problems.

Declaration of competing interest

The authors declare that they have no known competing financial interests or personal relationships that could have appeared to influence the work reported in this paper.

Acknowledgements

Appendix: Discontinuous Galerkin formulations

When considering the heat conduction in a two-dimensional square domain, the discontinuous Galerkin (DG) finite element method is applied to discretise the governing system on triangular meshes in the physical space. We present the detailed formulations in this section. Let $\Xi \in \mathbb{R}^2$ denoting a computational domain with boundary $\partial\Xi$ in the $x_1 - x_2$ plane, which is partitioned into N_{el} disjoint regular triangles $\Delta_l : \Xi = \cup_l^{N_{el}}\{\Delta_l\}$. The boundaries of the triangles define a group of N_{fc} faces $\Gamma_c : \Upsilon = \cup_l^{N_{el}}\{\partial\Delta_l\} = \cup_c^{N_{fc}}\{\partial\Gamma_c\}$. For the solution of the kinetic equation (16), approximations of the distribution function e are sought in the following piecewise finite element space

$$\mathcal{V} = \left\{ \psi_{el} : \psi_{el}|_{\Delta_l} \in \mathcal{P}^K(\Delta_l), \forall \Delta_l \subset \Xi \right\}, \tag{A.1}$$

where $\mathcal{P}^K(D)$ denotes the space of K-th order polynomials on a domain D. We introduce the notations $(a, b)_D = \int_{D \in \mathbb{R}^2} (a \odot b)\, \mathrm{d}x_1 \mathrm{d}x_2$ and $\langle a, b \rangle_D = \int_{D \in \mathbb{R}^1} (a \odot b)\, \mathrm{d}\Gamma$, where $\odot$ can be either the dot $(\cdot)$ or tensor $(\otimes)$ product. The DG formulation to find the approximations of e within each Δ_l at each iteration step is

$$\frac{1}{Kn_C} (\psi_{el}, e)_{\Delta_l} + \langle \psi_{el}, \hat{\boldsymbol{H}} \cdot \boldsymbol{n} \rangle_{\partial\Delta_l} - (\nabla\psi_{el}, \boldsymbol{v}e)_{\Delta_l} = \frac{1}{Kn_R} \left(\psi_{el}, e_{eq}^R\right)_{\Delta_l} + \frac{1}{Kn_N} \left(\psi_{el}, e_{eq}^N\right)_{\Delta_l}, \tag{A.2}$$

where $\boldsymbol{n}$ is the outward unit normal vector of $\partial\Delta_l$ and $\hat{\boldsymbol{H}}$ is the numerical flux that depends on the solutions from both sides of $\partial\Delta_l$ since the approximations of e are discontinuous there. We calculate the numerical flux using the first-order upwind principle as

$$\hat{\boldsymbol{H}} \cdot \boldsymbol{n} = \frac{1}{2}\boldsymbol{v} \cdot \boldsymbol{n}\, (e + e^*) + \frac{1}{2}|\boldsymbol{v} \cdot \boldsymbol{n}|\, (e - e^*), \tag{A.3}$$

with e^* being the distribution from a neighboring triangle that shares the boundary $\partial\Delta_l$ with Δ_l. If $\partial\Delta_l$ is at the boundary of computational domain, i.e. $\partial\Delta_l \cap \partial\Xi \neq 0$, e^* is evaluated using the given boundary condition. Once e^* is known, e in Δ_l can be obtained by solving the linear system (A.2). A sweeping technique is utilized to find e in an element-by-element fashion along the characteristic direction [55], i.e., direction of $\boldsymbol{v}$.

The synthetic macroscopic equations are solved by the hybridizable discontinuous Galerkin (HDG) method, where we first rewrite the steady-state governing equations (17)-(19) into the following mixed system

$$
\begin{aligned}
\boldsymbol{\mathcal{G}}_u + \nabla \cdot [\boldsymbol{\mathcal{G}}_c + \boldsymbol{\mathcal{G}}_d] &= 0, \\
\boldsymbol{P} - \frac{Kn_C}{5}\nabla\boldsymbol{q} + \boldsymbol{\Pi} &= 0,
\end{aligned}
\tag{A.4}
$$

where

$$
\boldsymbol{\mathcal{G}}_u = \begin{bmatrix} 0 \\ \frac{1}{Kn_R}\boldsymbol{q} \end{bmatrix}, \quad \boldsymbol{\mathcal{G}}_c = \begin{bmatrix} \boldsymbol{q} \\ \frac{T}{3}\boldsymbol{I} \end{bmatrix}, \quad \boldsymbol{\mathcal{G}}_d = \begin{bmatrix} \boldsymbol{0} \\ -\left(\boldsymbol{P} + \boldsymbol{P}^\top - \frac{2}{3}\mathrm{tr}\,(\boldsymbol{P})\,\boldsymbol{I}\right) \end{bmatrix}, \tag{A.5}
$$

and

$$
\boldsymbol{\Pi} = \tau_C \begin{bmatrix} \frac{\partial M_{111}}{\partial x_1} + \frac{\partial M_{112}}{\partial x_2} + \frac{1}{2}\left(\frac{\partial M_{221}}{\partial x_1} + \frac{\partial M_{222}}{\partial x_2}\right) & \frac{1}{2}\left(\frac{\partial M_{121}}{\partial x_1} + \frac{\partial M_{122}}{\partial x_2}\right) \\ \frac{1}{2}\left(\frac{\partial M_{121}}{\partial x_1} + \frac{\partial M_{122}}{\partial x_2}\right) & \frac{1}{2}\left(\frac{\partial M_{111}}{\partial x_1} + \frac{\partial M_{112}}{\partial x_2}\right) + \frac{\partial M_{221}}{\partial x_1} + \frac{\partial M_{222}}{\partial x_2} \end{bmatrix}, \tag{A.6}
$$

with $\boldsymbol{I}$ being the identity matrix and $\mathrm{tr}\,(\boldsymbol{P})$ denoting the (linear algebra) trace of $\boldsymbol{P}$. The auxiliary variable $\boldsymbol{P}$ is introduced to approximate the gradient of heat flux $\nabla\boldsymbol{q}$. As a result, the stress $N_{\langle ij \rangle}$ in (19) is equal to

$$
N_{\langle ij \rangle} = -\left(P_{ij} + P_{ji} - \frac{2}{3}P_{kk}\delta_{ij}\right). \tag{A.7}
$$

The quantities $\boldsymbol{M} = [T, \boldsymbol{q}]^\top$ as well as the auxiliary variable $\boldsymbol{P}$ are approximated within Δ_l in the finite element space $\mathcal{V}$; the traces of temperature and heat flux $\hat{\boldsymbol{M}} = \left[\hat{T}, \hat{\boldsymbol{q}}\right]^\top$, i.e., the values of these field variables on the faces Υ, are approximated in the following piecewise finite element space

$$
\mathcal{W} = \left\{\psi_{fc} : \psi_{fc}|_{\Gamma_c} \in \mathcal{P}^K\,(\Gamma_c)\,, \forall \Gamma_c \subset \Upsilon\right\}. \tag{A.8}
$$

It is assumed that $\hat{\boldsymbol{M}}$ are singled-valued on each face.

The HDG method solves the system in two steps: first, a global problem is set up to determine the traces $\hat{\boldsymbol{M}}$; then a local problem with $\hat{\boldsymbol{M}}$ as the boundary condition on $\partial\Delta_l$ is solved element-by-element to obtain the solutions for $\boldsymbol{M}$ and $\boldsymbol{P}$. The weak formulation for the local problem is to find $(\boldsymbol{M}, \boldsymbol{P}) \in [\mathcal{V}]^3 \times [\mathcal{V}]^4$ such that

$$
\begin{aligned}
(\boldsymbol{r}, \boldsymbol{\mathcal{G}}_u)_{\Delta_l} - (\nabla\boldsymbol{r}, \boldsymbol{\mathcal{G}}_c + \boldsymbol{\mathcal{G}}_d)_{\Delta_l} + \langle \boldsymbol{r}, \hat{\boldsymbol{F}} \cdot \boldsymbol{n}\rangle_{\partial\Delta_l} &= 0, \\
(\boldsymbol{t}, \boldsymbol{P})_{\Delta_l} + \frac{Kn_C}{5}(\nabla \cdot \boldsymbol{t}, \boldsymbol{q})_{\Delta_l} - \frac{Kn_C}{5}\langle \boldsymbol{t} \cdot \boldsymbol{n}, \hat{\boldsymbol{q}}\rangle_{\partial\Delta_l} &= (\boldsymbol{t}, \boldsymbol{\Pi})_{\Delta_l},
\end{aligned}
\tag{A.9}
$$

for all $(\boldsymbol{r}, \boldsymbol{t}) \in [\mathcal{V}]^3 \times [\mathcal{V}]^4$, where the numerical flux $\hat{\boldsymbol{F}}$ is defined as:

$$\hat{\boldsymbol{F}} \cdot \boldsymbol{n} = \left[\begin{array}{c} \hat{\boldsymbol{F}}_T \cdot \boldsymbol{n} \\ \hat{\boldsymbol{F}}_q \cdot \boldsymbol{n} \end{array} \right] = \left[\begin{array}{c} \boldsymbol{q} \\ \frac{1}{3}\hat{T} - \left(\boldsymbol{P} + \boldsymbol{P}^\top - \frac{2}{3}\mathrm{tr}\left(\boldsymbol{P}\right)\boldsymbol{I} \right) \end{array} \right] \cdot \boldsymbol{n} + \left[\begin{array}{c} T - \hat{T} \\ \boldsymbol{q} - \hat{\boldsymbol{q}} \end{array} \right]. \qquad (A.10)$$

The global problem is set up by enforcing the continuity of the numerical flux over all the interior faces. It is stated as: find $\hat{\boldsymbol{M}} \in [\mathcal{W}]^3$ such that

$$\left\langle \left(\hat{\boldsymbol{F}} \cdot \boldsymbol{n}\right)^+, \boldsymbol{w} \right\rangle_{\Gamma_c} + \left\langle \left(\hat{\boldsymbol{F}} \cdot \boldsymbol{n}\right)^-, \boldsymbol{w} \right\rangle_{\Gamma_c} = 0, \quad \text{on } \Gamma_c \in \Upsilon \backslash \partial\Xi, \qquad (A.11)$$

for all $\boldsymbol{w} \in [\mathcal{W}]^4$. Here the superscripts $\pm$ denote the numerical fluxes obtained from the triangles on both sides of the face. On boundary faces $\Gamma_c \in \Upsilon \cap \partial\Xi$, $\hat{\boldsymbol{M}}$ are determined from boundary conditions. In this paper, we consider two types of boundary condition: the Dirichlet condition where the given value of heat flux $\boldsymbol{q}_b$ is imposed on the Dirichlet boundary Υ_D so that

$$\langle \hat{\boldsymbol{q}} - \boldsymbol{q}_b, \boldsymbol{w} \rangle_{\Gamma_c} = 0, \quad \text{on } \Gamma_c \in \Upsilon_D, \qquad (A.12)$$

and the Neumann boundary Υ_N where the given value of temperature T_b is imposed on the Neumann boundary in a way analog to the pseudo traction on the Stokes flow [54] so that

$$\left\langle \left(\hat{\boldsymbol{F}}_q \cdot \boldsymbol{n}\right)^+ - \frac{T_b}{3}\boldsymbol{n}^+, \boldsymbol{w} \right\rangle_{\Gamma_c} = 0, \quad \text{on } \Gamma_c \in \Upsilon_N. \qquad (A.13)$$

Here we assume that for a boundary face, only the triangle on the '+' side exits.

On assembling the local problem (A.9) and the global problem (A.11) to (A.13) over all the triangles and faces, we can obtain a matrix system of form

$$\left[\begin{array}{ccc} A_M & A_P & A_{\hat{M}} \\ B_M & B_P & B_{\hat{M}} \\ Y_M & Y_P & Y_{\hat{M}} \end{array} \right] \left[\begin{array}{c} \mathbb{M} \\ \mathbb{P} \\ \hat{\mathbb{M}} \end{array} \right] = \left[\begin{array}{c} S_M \\ S_P \\ S_{\hat{M}} \end{array} \right], \qquad (A.14)$$

where $\mathbb{M}$, $\mathbb{P}$ and $\hat{\mathbb{M}}$ are the vectors of degrees of freedom of the field variables $\boldsymbol{M}$ and the auxiliary variable $\boldsymbol{P}$, as well as the traces of the field properties $\hat{\boldsymbol{M}}$, respectively. Note that the degrees of freedom for $\boldsymbol{M}$ and $\boldsymbol{P}$ are grouped together and ordered element-by-element. As a consequence, the corresponding coefficient matrix $[A_M, A_P; B_M, B_P]$ has block diagonal structure. Therefore, we can eliminate $\boldsymbol{M}$ and $\boldsymbol{P}$ to obtain a reduced linear system involving only $\hat{\mathbb{M}}$. Once $\hat{\mathbb{M}}$ is determined, $\boldsymbol{M}$ and $\boldsymbol{P}$ are reconstructed corresponding to the local problem (A.9) in an element-wise fashion. In this paper the reduced linear system for $\hat{\mathbb{M}}$ is solved by the direct solver PARDISO [56].

References

[1] D. G. Cahill, W. K. Ford, K. E. Goodson, G. D. Mahan, A. Majumdar, H. J. Maris, R. Merlin, S. R. Phillpot, Nanoscale thermal transport, Journal of Applied Physics 93 (2) (2003) 793–818.

[2] D. G. Cahill, P. V. Braun, G. Chen, D. R. Clarke, S. Fan, K. E. Goodson, P. Keblinski, W. P. King, G. D. Mahan, A. Majumdar, et al., Nanoscale thermal transport. II. 2003–2012, Applied Physics Reviews 1 (1) (2014) 011305.

[3] G. Chen, Non-Fourier phonon heat conduction at the microscale and nanoscale, Nature Reviews Physics 3 (8) (2021) 555–569.

[4] H. Bao, J. Chen, X. Gu, B. Cao, A review of simulation methods in micro/nanoscale heat conduction, ES Energy & Environment 1 (2018) 16–55.

[5] J. Y. Murthy, S. V. J. Narumanchi, J. A. Pascual-Gutierrez, T. Wang, C. Ni, S. R. Mathur, Review of multiscale simulation in submicron heat transfer, International Journal for Multiscale Computational Engineering 3 (1) (2005) 5–32.

[6] X. Gu, Y. Wei, X. Yin, B. Li, R. Yang, Colloquium: phononic thermal properties of two-dimensional materials, Reviews of Modern Physics 90 (2018) 041002.

[7] Z. Zhang, Y. Ouyang, Y. Cheng, J. Chen, N. Li, G. Zhang, Size-dependent phononic thermal transport in low-dimensional nanomaterials, Physics Reports 860 (2020) 1–26.

[8] G. Chen, Nanoscale energy transport and conversion: a parallel treatment of electrons, molecules, phonons, and photons, Oxford university press, 2005.

[9] M. Kaviany, Heat transfer physics, Cambridge University Press, 2008.

[10] C. C. Ackerman, B. Bertman, H. A. Fairbank, R. A. Guyer, Second sound in solid helium, Physical Review Letter 16 (1966) 789–791.

[11] H. Beck, P. F. Meier, A. Thellung, Phonon hydrodynamics in solids, Physica Status Solidi A 24 (1) (1974) 11–63.

[12] Y. Guo, M. Wang, Phonon hydrodynamics and its applications in nanoscale heat transport, Physics Reports 595 (2015) 1–44.

[13] C. Yu, Y. Ouyang, J. Chen, A perspective on the hydrodynamic phonon transport in two-dimensional materials, Journal of Applied Physics 130 (1) (2021) 010902.

[14] S. Huberman, R. A. Duncan, K. Chen, B. Song, V. Chiloyan, Z. Ding, A. A. Maznev, G. Chen, K. A. Nelson, Observation of second sound in graphite at temperatures above 100 K, Science 364 (6438) (2019) 375–379.

[15] J. Callaway, Model for lattice thermal conductivity at low temperatures, Physical Review 113 (4) (1959) 1046.

[16] R. A. Guyer, J. A. Krumhansl, Solution of the linearized phonon Boltzmann equation, Physical Review 148 (2) (1966) 766.

[17] S. Chapman, T. G. Cowling, C. Cercignani, The mathematical theory of non-uniform gases: an account of the kinetic theory of viscosity, thermal conduction, and diffusion in gases, 3rd Edition, Cambridge Mathematical Library, Cambridge University Press, 1995.

[18] D. D. Joseph, L. Preziosi, Heat waves, Reviews of Modern Physics 61 (1989) 41–73.

[19] Z. Banach, W. Larecki, Chapman–Enskog method for a phonon gas with finite heat flux, Journal of Physics A: Mathematical and Theoretical 41 (37) (2008) 375502.

[20] M. J. Fryer, H. Struchtrup, Moment model and boundary conditions for energy transport in the phonon gas, Continuum Mechanics and Thermodynamics 26 (5) (2014) 593–618.

[21] M. Simoncelli, N. Marzari, A. Cepellotti, Generalization of Fourier's law into viscous heat equations, Physical Review X 10 (2020) 011019.

[22] L. Sendra, A. Beardo, P. Torres, J. Bafaluy, F. X. Alvarez, J. Camacho, Derivation of a hydrodynamic heat equation from the phonon Boltzmann equation for general semiconductors, Physical Review B 103 (2021) L140301.

[23] S. Mazumder, A. Majumdar, Monte Carlo study of phonon transport in solid thin films including dispersion and polarization, Journal of Heat Transfer 123 (4) (2001) 749–759.

[24] X. Li, S. Lee, Crossover of ballistic, hydrodynamic, and diffusive phonon transport in suspended graphene, Physical Review B 99 (2019) 085202.

[25] B.-D. Nie, B.-Y. Cao, Thermal wave in phonon hydrodynamic regime by phonon Monte Carlo simulations, Nanoscale and Microscale Thermophysical Engineering 24 (2) (2020) 94–122.

[26] A. Christensen, S. Graham, Multiscale lattice Boltzmann modeling of phonon transport in crystalline semiconductor materials, Numerical Heat Transfer, Part B: Fundamentals 57 (2) (2010) 89–109.

[27] S. A. Ali, G. Kollu, S. Mazumder, P. Sadayappan, A. Mittal, Large-scale parallel computation of the phonon Boltzmann transport equation, International Journal of Thermal Sciences 86 (2014) 341 – 351.

[28] R. Yang, G. Chen, M. Laroche, Y. Taur, Simulation of nanoscale multidimensional transient heat conduction problems using ballistic-diffusive equations and phonon Boltzmann equation, Journal of Heat Transfer 127 (3) (2005) 298–306.

[29] Z. Guo, K. Xu, Discrete unified gas kinetic scheme for multiscale heat transfer based on the phonon Boltzmann transport equation, International Journal of Heat and Mass Transfer 102 (2016) 944–958.

[30] X.-P. Luo, Y.-Y. Guo, M.-R. Wang, H.-L. Yi, Direct simulation of second sound in graphene by solving the phonon Boltzmann equation via a multiscale scheme, Physical Review B 100 (15) (2019) 155401.

[31] J.-P. M. Péraud, N. G. Hadjiconstantinou, Efficient simulation of multidimensional phonon transport using energy-based variance-reduced Monte Carlo formulations, Physical Review B 84 (20) (2011) 205331.

[32] Z. Guo, C. Shu, Lattice Boltzmann method and its applications in engineering, Vol. 3, World Scientific, 2013.

[33] J. M. Loy, J. Y. Murthy, D. Singh, A fast hybrid Fourier–Boltzmann transport equation solver for nongray phonon transport, Journal of Heat Transfer 135 (1) (2012) 011008–011008.

[34] J. M. Loy, S. R. Mathur, J. Y. Murthy, A coupled ordinates method for convergence acceleration of the phonon Boltzmann transport equation, Journal of Heat Transfer 137 (1) (2015) 012402.

[35] C. Zhang, Z. Guo, S. Chen, Unified implicit kinetic scheme for steady multiscale heat transfer based on the phonon Boltzmann transport equation, Physical Review E 96 (6) (2017) 063311.

[36] C. Zhang, Z. Guo, S. Chen, An implicit kinetic scheme for multiscale heat transfer problem accounting for phonon dispersion and polarization, International Journal of Heat and Mass Transfer 130 (2019) 1366–1376.

[37] M. L. Adams, E. W. Larsen, Fast iterative methods for discrete-ordinates particle transport calculations, Progress in Nuclear Energy 40 (1) (2002) 3–159.

[38] J. R. Harter, S. A. Hosseini, T. S. Palmer, P. A. Greaney, Prediction of thermal conductivity in dielectrics using fast, spectrally-resolved phonon transport simulations, International Journal of Heat and Mass Transfer 144 (2019) 118595.

[39] D. Terris, K. Joulain, D. Lemonnier, D. Lacroix, Modeling semiconductor nanostructures thermal properties: The dispersion role, Journal of Applied Physics 105 (7) (2009) 073516.

[40] H. J. Kopp, Synthetic method solution of the transport equation, Nuclear Science and Engineering 17 (1) (1963) 65–74.

[41] C. Zhang, S. Chen, Z. Guo, L. Wu, A fast synthetic iterative scheme for the stationary phonon Boltzmann transport equation, International Journal of Heat and Mass Transfer 174 (2021) 121308.

[42] W. Su, L. Zhu, P. Wang, Y. Zhang, L. Wu, Can we find steady-state solutions to multiscale rarefied gas flows within dozens of iterations?, Journal of Computational Physics 407 (2020) 109245.

[43] W. Su, Y. Zhang, L. Wu, Multiscale simulation of molecular gas flows by the general synthetic iterative scheme, Computer Methods in Applied Mechanics and Engineering 373 (2021) 113548.

[44] L. Zhu, X. Pi, W. Su, Z.-H. Li, Y. Zhang, L. Wu, General synthetic iterative scheme for nonlinear gas kinetic simulation of multi-scale rarefied gas flows, Journal of Computational Physics 430 (2021) 110091.

[45] R. Yang, S. Yue, B. Liao, Hydrodynamic phonon transport perpendicular to diffuse-gray boundaries, Nanoscale and Microscale Thermophysical Engineering 23 (1) (2019) 25–35.

[46] W. Dreyer, H. Struchtrup, Heat pulse experiments revisited, Continuum Mechanics and Thermodynamics 5 (1) (1993) 3–50.

[47] A. Cepellotti, G. Fugallo, L. Paulatto, M. Lazzeri, F. Mauri, N. Marzari, Phonon hydrodynamics in two-dimensional materials, Nature Communications 6 (1) (2015) 6400.

[48] R. A. Guyer, J. A. Krumhansl, Thermal conductivity, second sound, and phonon hydrodynamic phenomena in nonmetallic crystals, Physical Review 148 (1966) 778–788.

[49] C. Zhang, S. Chen, Z. Guo, Heat vortices of ballistic and hydrodynamic phonon transport in two-dimensional materials, International Journal of Heat and Mass Transfer 176 (2021) 121282.

[50] A. Majumdar, Microscale heat conduction in dielectric thin films, Journal of Heat Transfer 115 (1) (1993) 7–16.

[51] S. Lee, D. Broido, K. Esfarjani, G. Chen, Hydrodynamic phonon transport in suspended graphene, Nature Communications 6 (1) (2015) 6290.

[52] W. Su, L. Zhu, L. Wu, Fast convergence and asymptotic preserving of the general synthetic iterative scheme, SIAM Journal on Scientific Computing 42 (6) (2020) B1517–B1540.

[53] Y. Guo, M. Wang, Heat transport in two-dimensional materials by directly solving the phonon Boltzmann equation under Callaway's dual relaxation model, Physical Review B 96 (13) (2017) 134312.

[54] R. Sevilla, A. Huerta, HDG-NEFEM with degree adaptivity for Stokes flows, Journal of Scientific Computing 77 (2018) 1953–1980.

[55] W. Su, P. Wang, Y. Zhang, L. Wu, Implicit Discontinuous Galerkin method for the Boltzmann equation, Journal of Scientific Computing 82 (2020) 39.

[56] O. Schenk, K. Gärtner, Solving unsymmetric sparse systems of linear equations with PARDISO, Future Generation Computer Systems 20 (3) (2004) 475 – 487, selected numerical algorithms.